Journal of Power Sources 435 (2019) 226768

Contents lists available at ScienceDirect

Journal of Power Sources

journal homepage: www.elsevier.com/locate/jpowsour

Multi-functional transparent electrode for reliable flexible perovskite solar cells

Gill Sang Han [a,b,1], Seongha Lee [a,1], Matthew Lawrence Duff [a], Fen Qin [a], Minlin Jiang [c], Guangyong Li [d], Jung-Kun Lee [a,*]

[a] Department of Mechanical Engineering and Materials Science, University of Pittsburgh, PA, 15216, USA
[b] School of Advanced Materials Science and Engineering, Sungkyunkwan University, Suwon, 16419, Republic of Korea
[c] Institute for Advanced Study, Nanchang University, Nanchang, Jiangxi, 330031, China
[d] Department of Electrical and Computer Engineering, University of Pittsburgh, PA, 15216, USA

HIGHLIGHTS

- $MoO_x/Ag/MoO_x$ multilayer is used as a top electrode of perovskite solar cells.
- The multilayer electrode has multiple functions in real operation environment.
- 92% of the initial current density is maintained after 24 h continuous operation.
- The efficiency of flexible solar cells using $MoO_x/Ag/MoO_x$ reaches 14.5%.

GRAPHICAL ABSTRACT

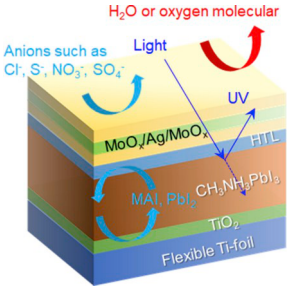

ARTICLE INFO

Keywords:
Flexible perovskite solar cell
Long-term stability
Dielectric/metal/dielectric
Photo-degradation

ABSTRACT

Multilayer $MoO_x/Ag/MoO_x$ (DMD) films are found to be transparent conducting electrodes for use in extremely stable and highly bendable flexible perovskite solar cells (PSCs). The optical transparency and electric properties of DMD and its role as a top electrode of PSCs were studied by changing the thickness of the MoO_x layer. Although the MoO_x thickness was shown to have a negligible effect on the sheet resistance of DMD, the transmittance of visible light, selective carrier transport capability, and long-term stability of a device considerably depend on this factor. The sandwich structure of a 20-nm-thick MoO_x, 7-nm-thick Ag, and 20-nm-thick MoO_x exhibits a high transmittance and large photon–electron conversion rate of PSCs. In addition, PSCs using the DMD top electrode maintain 92% of their initial current density after 24 h of continuous operation owing to a UV light cut-off of the top illumination. Moreover, the overall structure of DMD blocks the diffusion of water and oxygen molecules from real environmental conditions. At the same time, the underlying/upper MoO_x layer retards the degradation through a chemical reaction between Ag and the halide ions inside the cells, as well as foreign ions from outside the polluted atmosphere. When DMD is applied to flexible PSCs on Ti foil, the PCE reaches 14.5%, and mechanical integrity of the PSCs is maintained at a bending radius of 4 mm.

* Corresponding author.
E-mail address: jul37@pitt.edu (J.-K. Lee).
[1] These authors contributed equally to this work.

https://doi.org/10.1016/j.jpowsour.2019.226768
Received 5 March 2019; Received in revised form 11 May 2019; Accepted 17 June 2019
Available online 24 June 2019

1. Introduction

Emerging solar cells are composed of unique light absorbers such as dyes, organic semiconductors, inorganic quantum dots, and organic-inorganic hybrid perovskite materials. They feature both a low cost and high efficiency. Among these emerging solar cells, perovskite solar cells (PSCs) are the most promising candidates for next-generation solar cells and have been extensively studied during the past six years. After the rapid improvement over the last several years, the highest power conversion efficiency (PCE) yet achieved was ~24.2%, which is much higher than the PCE of other emerging solar cells [1]. Therefore, the current major requirements for PSCs in replacing a portion of the Si solar cell market are not associated with PCEs but are instead related to the chemical stability, large-scale manufacturing, and benign nature of the components. To address these problems, many derivatives of a representative perovskite material $(CH_3NH_3)PbI_3$ have been developed. Different amidinium cations, alkali cations, and halogen anions have been applied [2–5]. Although these mixed and doped materials have shown improvements in their stability, the degradation problem of hybrid perovskite materials has yet to be completely resolved. When hybrid perovskite materials are exposed to water, UV light, or oxygen at ~100 °C, the materials easily dissociate into hexagonal iodide and release the residual gas.

In addition to changing the composition of the perovskite material, researchers have employed several strategies to enhance the stability of PSCs under normal ambient conditions. First, the surface treatment of an electron-transport layer, TiO_2, can retard the decomposition of the perovskite materials and prevent the trapping of mobile ions at the interface between the perovskite and TiO_2 layers [6–8]. Second, *n*-type oxide semiconductors such SnO_2 and ZnO have been chosen as an electron-transport layer [9–11]. Third, the device structure of PSCs has changed, and an inverted design of PSCs with a *p-i-n* structure has been proposed to avoid the photocatalytic effect of UV irradiation [12,13]. Fourth, an encapsulation layer made up of a coated or glass plate is sealed on top of the PSCs to protect the perovskite materials [14,15]. The encapsulation layer or glass prevents water and oxygen from reaching the perovskite layer. For example, a composite of poly(methyl methacrylate) (PMMA) and reduced graphene oxide (rGO) operates as a hydrophobic coating layer, which increases the chemical and thermal stability of the perovskite material in humid and hot environments [15].

In this study, we report a design rule of a multi-functional transparent electrode for use in stable and efficient PSCs by combining both experimental and theoretical methods. Multilayer dielectric material/metal/dielectric (DMD) such as MoO_3/Au/MoO_3 was recently used as an intermediate transparent electrode in a tandem solar cell employing PSCs [16–18]. Very recently, it was found that a SnO_2/Ag/SnO_2 (SAS) layer protects the perovskite layer of PSCs for up to 4500 h at 60 °C in a nitrogen atmosphere [19,20]. However, in previous studies, solar light hits the DMD after passing through the PSCs, and the effect of the optical transparency and electric conductivity of DMD on the PCE and stability of PSCs has yet to be systematically explored. We modified the individual layer of DMD to increase the PCE and stability of the PSCs under the top illumination mode. In comparison to traditional PSCs, UV light does not pass through the TiO_2 layer or perovskite/TiO_2 interface under this mode. Before UV light reaches TiO_2, the dielectric layer of the DMD electrodes and hole-transport layer (HTL) absorb UV light, and the photocatalytic decomposition of the perovskite layer is suppressed. Therefore, the PSCs of the DMD do not show a change in PCE for 24 h under humid air conditions. It was found that a sandwich MoO_x structure can retard the diffusion of water or oxygen molecules from the atmosphere, blocking the reaction of Ag with other anions and absorbing UV light. When a DMD electrode is applied to flexible PSCs on Ti foil, the PCE exhibited 14.5% which is higher than PCE of previous PSCs under the top illumination (Table S1). In addition, the mechanical integrity of the PSCs is maintained at a bending radius of 4 mm and no change in PCE is observed in bent PSCs on Ti foil. These results indicate that a dielectric/metal/dielectric layer is not only a good transparent electrode but also a passivation layer for PSCs without incurring any photodegradation.

2. Results and discussion

Fig. 1a shows a schematic of the structure of PSCs coated with a multilayer transparent electrode. Here, MoO_x was chosen as the dielectric component of the DMD electrode because the band alignment at the interface of the MoO_x and Sprio-OMeTAD forces holes to flow from the Sprio-OMeTAD to the MoO_x and blocks the electron transfer toward the MoO_x. Owing to its higher affordability than Au, Ag was selected as a central layer of the sandwich DMD structure. In prior studies, Ag was tested as the metal electrode of PSCs. However, it was found that Ag easily reacts with halide and destabilizes the hybrid perovskite layer. Fig. 1b shows a cross-sectional SEM image of PSCs built on a commercial FTO/glass substrate. A hole-blocking TiO_2 layer (*b*-TiO_2) with a thickness of ~50 nm and TiO_2 NPs with a thickness of ~200 nm were used as a hole-blocking layer and an electron-transport layer, respectively. In addition, HTL (Sprio-OMeTAD) was deposited on top of the ~500 nm thick $CH_3NH_3PbI_3$ perovskite layer. A MoO_x layer with a thickness of 10–30 nm was deposited on the Spiro-OMeTAD layer, and a 7-nm-thick layer of Ag was deposited on the MoO_x layer. Another 10–30 nm thick MoO_x layer was then deposited. This DMD electrode design was guided based on a finite-difference time-domain (FDTD) simulation to maximize the transmittance of visible light. The optical interference between MoO_x and Ag at two MoO_x–Ag interfaces increases the optical transparency of the DMD electrode.

Fig. 2a shows *J-V* curves of PSCs when simulated solar light (AM 1.5 condition) first passes through the DMD electrode before reaching the hybrid perovskite layer (called the top illumination layer). The mean values of the short current density (J_{sc}), open circuit voltage (V_{oc}), fill

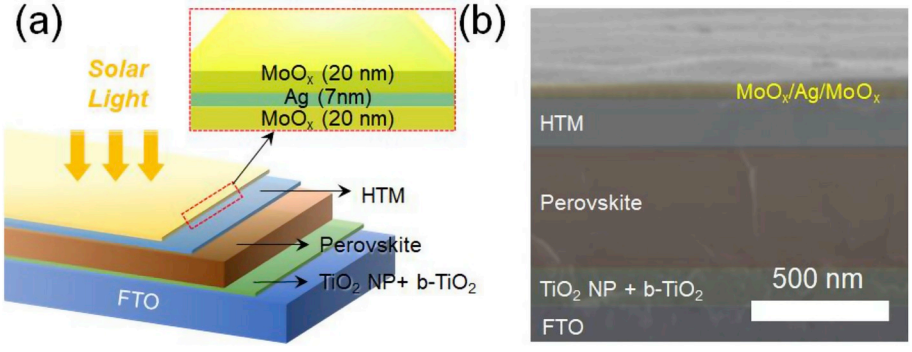

Fig. 1. (a) Schematic and (b) cross-sectional SEM image of dielectric/metal/dielectric DMD structure composed of MoO_x/Ag/MoO_x/HTM/$CH_3NH_3PbI_3$/mp-TiO_2/bl-TiO_2/FTO.

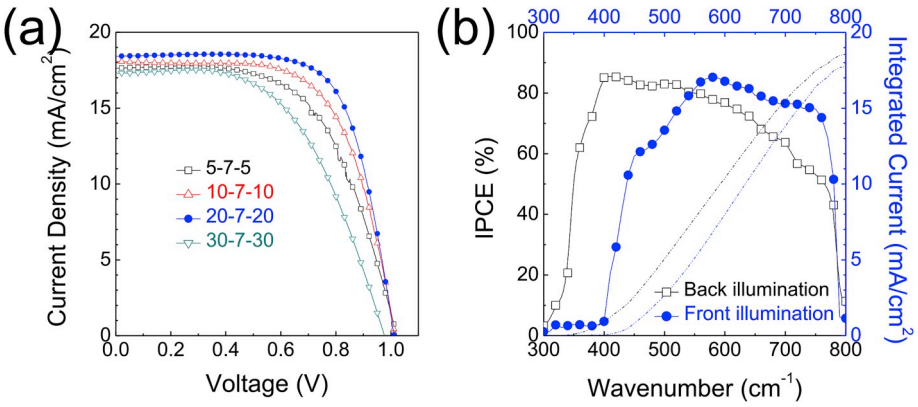

Fig. 2. (a) *J-V* curves of MoO_x/Ag/MoO_x/HTM/$CH_3NH_3PbI_3$/TiO_2/FTO cells at 1.5 a.m. illumination as a function of MoO_x thickness, and (b) IPCE of PSCs with MoO_x (20 nm)/Ag (7 nm)/MoO_x (20 nm).

Table 1
Represented photovoltaic properties of PSCs with MoO_x/Ag/MoO_x, as a function of MoO_x thickness.

MoO_x/Ag/MoO_x (Layer thickness in nm)	J_{sc} (mA/cm^2)	V_{oc} (V)	FF	*PCE* (%)
5-7-5	17.55 ±0.51	1.017 ±0.006	0.60 ±0.05	10.78 ±1.10
10-7-10	17.83 ±0.32	1.003 ±0.009	0.65 ±0.03	11.61 ±0.65
20-7-20	18.29 ±0.41	1.003 ±0.005	0.68 ±0.02	12.45 ±0.96
30-7-30	17.78 ±0.50	0.980 ±0.004	0.54 ±0.01	9.80 ±0.73

factor (*ff*), and power conversion efficiency (PCE) of the PSCs using different MoO_x/Ag/MoO_x electrodes are summarized in Table 1. Only the thickness of the MoO_x layer was changed to modify the optical and electric properties of the DMD electrode; whereas, the thickness of the Ag layer was fixed at 7 nm to minimize light attenuation and maintain the good electric conductivity of the DMD electrode. Because Sprio-OMeTAD cannot be easily deposited on glass owing to its poor wetting property, only the overall transmittance of DMD/Spiro-OMeTAD was simulated. The results of the FDTD simulation are shown in Fig. S1a, which indicates that the theoretical current of PSCs from the top illumination through the DMD electrode is 20.85 mA cm^{-2}. The sheet resistance of DMD films with different MoO_x thicknesses is ~40 Ω cm^{-2}, regardless of the MoO_x thickness (Table S2). This indicates that the electric resistance of DMD films is mainly determined by the Ag layer thickness.

Table 1 shows that average PCE of PSCs using DMD top electrodes of 5/7/5, 10/7/10, 20/7/20, and 30/7/30 nm is 10.9%, 11.8%, 12.9%, and 9.31%, respectively. The best PCE is obtained in PSCs with a DMD of 20/7/20 nm. The change in PCE is attributed to the changes in J_{sc} and FF. In addition, J_{sc} gradually increases to 18.3 mA cm^{-2} as the thickness of MoO_x increases to 20 nm. The average J_{sc} for a DMD of 20/7/20 mm is 88% of the theoretical limit (20.85 mA cm^{-2}), which suggests that MoO_x adheres well to the other layers and has a good hole selection capability. Fig. 2b shows IPCE spectra of PSCs for a DMD of 20/7/20 nm. Light is illuminated from the DMD (top illumination) and glass (back illumination) sides. The integrated J_{sc} of the top illumination mode is smaller than that of the back-illumination mode by ~3.2 mA cm^{-2}. However, under top illumination mode, the IPCE of the PSCs begins decreasing at a wavelength of 420 nm and reaches approximately zero within the UV region, which is due to the filtering of UV light by spiro-OMeTAD. This suggests that the degradation of the PSCs by UV light can be suppressed under top illumination mode. The effects of the DMD electrode on the long-term stability of the PSCs are further discussed in the following section. To understand the effect of the MoO_x thickness, the *J-V* curves, shown in Fig. 2a are fitted using a standard diode equation for solar cells. Fig. S2 shows the series resistance of PSCs with a MoO_x layer of a different thickness. When DMD electrodes of 5/7/5, 10/7/10, and 20/7/20 mm are applied, the series resistances (R_s) of the PSCs are 5.3, 4.0, and 3.6 Ω cm^2, respectively. However, R_s of the PSCs for DMD of 30/7/30 mm is 3-times larger than that for DMD of 20/7/20 mm. This explains why the PSCs for DMD of 30/7/30 mm has the lowest FF (0.59). Although DMD electrodes of 20/7/20 and 30/7/30 mm have a similar sheet resistance for electron transport, the hole transfer from Ag (work function of ~4.2 eV) to MoO_x (work function of ~6 eV) is not favorable, and an increase in the MoO_x thickness results in the full development of a Schottky barrier for holes at one of the Ag–MoO_x interfaces. A similar thickness effect was recently reported for photovoltaics [21,22]. DMD of 20/7/20 mm has a high transmittance, large electric conductivity, and low Schottky barrier for hole transport.

One important observation of this study is that the PSCs of DMD exhibit very high long-term stability over continuous light illumination. Fig. 3a schematically describes the effect of a DMD electrode. First, in top illumination mode, the MoO_x and HTL layers absorb UV light and prevent photocatalytic decomposition of the hybrid perovskite material. Second, because a DMD electrode covers the entire top surface of the HTL layer, the electrode operates as an encapsulation layer to protect the perovskite layer from the ambiance. Third, the MoO_x layer retards the corrosive reaction of Ag with the halide ions of the hybrid perovskite layer and the oxidation of Ag in ambient air [23]. Fig. 3b shows that the sheet resistance of a thin Ag layer without an upper MoO_x layer increases by ~430% when the electrode is stored in ambient air (temperature of 20 ± 3 °C, relative humidity of 45 ± 5%) for a period of one month. In contrast, the 20 nm thick MoO_x upper layer protects the thin Ag interlayer from degradation for up to one month. The light stability of the PSCs of a DMD electrode was also tested in ambient air conditions (temperature of 20 ± 3 °C, relative humidity of 45 ± 5%). PSCs were illuminated continuously in top illumination mode while a bias of 0.8 V was applied. Fig. 3c shows the normalized J_{sc}. After a 24 h aging test, the PSCs of the DMD electrode possess 92% of the initial J_{sc} and do not show any color change of the hybrid perovskite layer. To compare the light stability, a control PSC was fabricated using an ~80 nm Au electrode deposited on top of the Sprio-OMeTAD layer, and light was illuminated from the glass side of the PSCs. After 20 h of continuous back illumination, the J_{sc} of the control PSCs decreased by 99%. In addition, the color of the hybrid perovskite layer changed from dark brown to yellow.

To better understand the degradation of the hybrid perovskite by UV light, we carried out an admittance spectroscopy examination of fresh and degraded PSCs [24]. The degraded PSC was continuously exposed to UV light for 12 h. Fig. 4a shows an Arrhenius plot of the characteristic frequency over temperature.

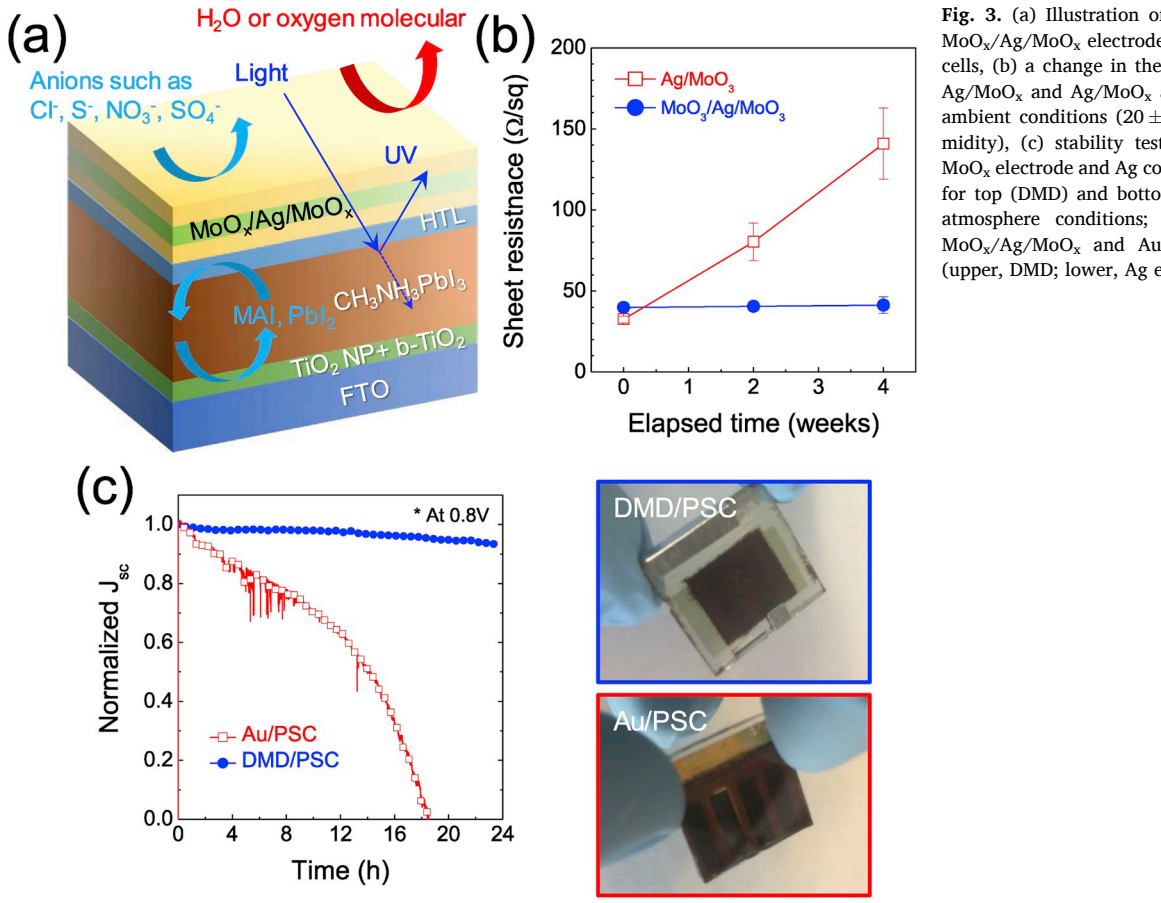

Fig. 3. (a) Illustration of multi-functional effect of $MoO_x/Ag/MoO_x$ electrode on top of perovskite solar cells, (b) a change in the sheet resistance of $MoO_x/Ag/MoO_x$ and Ag/MoO_x as a function of age under ambient conditions (20 ± 3 °C, 45 ± 5% relative humidity), (c) stability test of PSCs with $MoO_x/Ag/MoO_x$ electrode and Ag continuing to operate at 0.8 V for top (DMD) and bottom (Au) illumination under atmosphere conditions; photograph of PSC with $MoO_x/Ag/MoO_x$ and Au after operating for 24 h (upper, DMD; lower, Ag electrode).

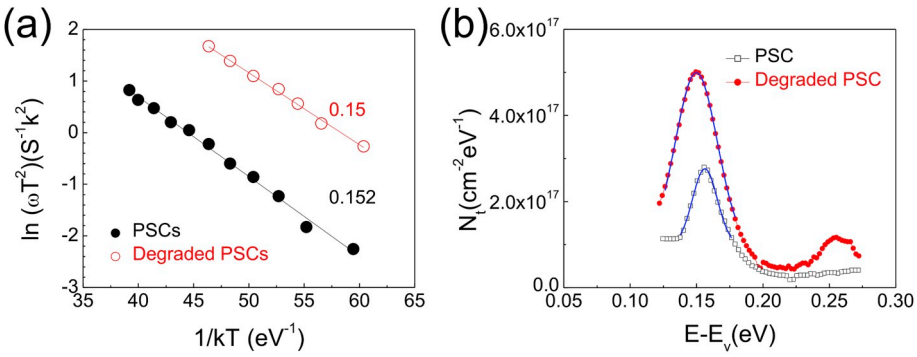

Fig. 4. Deep level transient spectroscopy of PSCs: (a) Arrhenius plots of the characteristic frequencies and (b) defect energy distribution of PSCs before/after degradation by light soaking. The slope indicates a deep trap energy of 0.15 eV, which contributes to iodine interstitials [24].

$$\omega_0 = 2DT^2 exp\left(-\frac{E_a}{kT}\right)$$

where ω_0 indicates the characteristic transition frequency, D is a constant related to the effective density of the states in the conduction band, and T is the temperature. Both PSCs have a similar defect energy of ~0.15 eV, which is assigned as iodine interstitials with lower energy traps. However, they have a different defect density, as shown in Fig. 4b [25–27]. The integrated defect density of the control PSC is $\sim 9.51 \times 10^{15}$ cm^{-3}, which is comparable to the reported values [26]. In contrast, the defect density was doubled in the degraded PSC (2.16×10^{16} cm^{-3}). This indicates that the illumination does not produce any new types of defects in the hybrid perovskite but increases the density of the existing major defects. Fig. S3 shows the XRD patterns of the PSCs of a DMD. One PSC was illuminated from the glass side, and the other was illuminated from the DMD side. Only the degraded PSC that was illuminated from the glass side exhibited a peak at $2\theta = 12.6°$. This peak corresponds to the (001) plane of PbI_2, which is evidence of the dissociation of $CH_3NH_3PbI_3$ by UV light. This indicates that the DMD layer can successfully prevent the photocatalytic decomposition and penetration of contaminants from the ambient air.

One promising application of a DMD top electrode is a flexible solar cell, which requires a highly conductive and transparent electrode. We tested a DMD electrode in Ti foil-based PSCs, which were recently reported [28]. A TiO_2 layer thermally grown on a Ti plate can be an excellent electron-transport layer for flexible PSCs of high PCE and good mechanical properties. Fig. 5a shows the *J-V* curve of the best performing PSCs on Ti foil. The DMD top electrode was deposited as the top

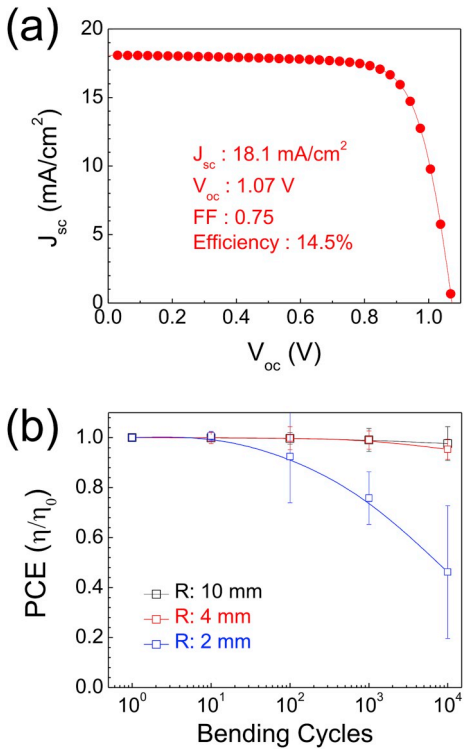

Fig. 5. (a) Best-performing *J-V* curve for MoO_x/Ag/MoO_x based PSCs on Ti metal plate and (b) change in normalized PCE of MoO_x/Ag/MoO_x based PSCs on Ti metal plate during repeated bending with different bending radii at 2, 4, and 10 mm, respectively.

electrode, and light was illuminated from the DMD side. The values of J_{sc}, V_{oc}, *ff*, and *PCE* are 18.1 mA cm^{-2}, 1.07 V, 0.75, and 14.5%, respectively. In comparison to the PSCs of TiO_2 nanoparticles, a higher V_{oc} of the flexible PSCs is attributed to the fact that the thermal oxidation of the Ti foil improves the crystalline quality of the TiO_2 layer, decreases the defect concentration and electron density, and increases the Fermi energy level of the TiO_2 layer. The mechanical endurance of the flexible PSCs of the DMD top electrodes was examined through the repeated bending of the PSCs at different radii of curvature (R). The results of this are shown in Fig. 5b. Even after bending 10,000 times at $R = 4$ mm, the PCE of the PSCs maintains 96% of the initial value. This stable mechanical endurance is due to a stacking of the metal and oxide layers. Whereas a pure oxide layer such as an ITO film on a PEN sheet is easily broken during the bending test [29], the interface between the MoO_x and Ag prevents the propagation of cracks, and the defects are confined in MoO_x. This retards the failure of the DMD film and increases the bending capability of the PSCs.

3. Conclusion

We investigated the optical and electric properties of a DMD multilayer film (MoO_x – Ag – MoO_x) and tested its performance as a multifunctional top electrode of PSCs. A change in the thickness of the MoO_x layer controls the optical transparency and hole-transport behavior of a DMD electrode. A DMD film consisting of 20-nm-thick MoO_x, 7-nm-thick Ag, and 20-nm-thick MoO_x layers results in the best performance from the viewpoint of solar energy harvesting and long-term stability. In addition to working as a transparent conducting electrode, the DMD top electrode filters UV light, passivates the hybrid perovskite layer from the ambient air, and hinders the corrosive reaction of Ag with halide ions. This self-encapsulated electrode was applied to the flexible PSCs of a Ti foil. The best PCE of the flexible PSC of the DMD electrode was shown to be 14.5%, which did not vary during the mechanical bending test. Our results suggest that a DMD film is a promising and multi-functional transparent electrode for use with PSCs.

4. Experimental

4.1. Device fabrication

FTO (NSG TECTM 8.8 Ω/sq) coated glass was cut into pieces of 2×2 cm^2 in size and partially etched with zinc powder and hydrochloric acid. The substrates were thoroughly cleaned with acetone, deionized (DI) water, and ethanol for 15 min, sequentially. UV-ozone was used to remove organic residue on the FTO. A TiO_2 blocking layer (bl-TiO_2) was spin-coated onto the FTO substrate at 4000 rpm for 30 s using a prepared 0.15 M titanium diisopropoxide bis-(acetylacetonate) in 1-butanol followed by annealing in a box furnace at 500 °C for 30 min. The substrate was immersed in an aqueous $TiCl_4$ solution for 30 min at 72 °C and annealed in the box furnace at 500 °C for 30 min. Mesoporous-TiO_2 nanoparticles diluted in a TiO_2 paste in ethanol (1:5.5 wt%, Sharechem) were spin-coated onto the bl-TiO_2/FTO substrate at 5000 rpm for 30 s followed by annealing at 550 °C for 30 min. After cooling to room temperature, a $CH_3NH_3PbI_3$ perovskite layer was formed on the $TiCl_4$ treated mesoporous TiO_2 layer in a one-step manner using an adduct method. To prepare the $CH_3NH_3PbI_3$ solution, PbI_2, CH_3NH_3I, and DMSO (1:1:1: M ratio) were dissolved in a *N*,*N*-dimethylforDMDide (DMF) solvent for 30 min and spin-coated at 4000 rpm for 25 s, and diethyl ether was then dropped during the spin-coating procedure. The substrate was then annealed at 65 °C for 3 min and at 100 °C for 10 min. The HTL solution was prepared by dissolving 36 mg of 2,2′,7,7′-tetrakis [*N*,*N*-di(4-methoxyphenyl)-amino]-9,9′-spirobi-fluorene (spiro-OMeTAD) in 500 μL of chlorobenzene, 14.4 μL of 4-*tert*-butyl pyridine, and 8.8 μL of lithium-bis(trifluoro-methanesulfonyl)-imide (Li-TFSI) in acetonitrile (720 mg ml^{-1}). The solution was spin-coated on the perovskite/mp-TiO_2/bl-TiO_2/FTO at 4000 rpm for 30 s. Finally, a 20-nm-thick MoO_x, 7-nm-thick Ag, and 20-nm-thick MoO_x were deposited using e-beam evaporation on the top of the HTL as a transparent top electrode.

4.2. Preparation of Ti metal plate for flexible PSCs

The thin TiO_2 as an ETL was prepared using a thermal oxidation process on a Ti metal plate, as previously reported in our group [28]. Ti metal plates were cleaned in aceton, deionized water, and ethanol for 20 min separately. After cleaning, Ti metal plates were annealed at 500 °C for 24 h. The oxidized TiO_2 was then annealed at 400 °C for 1 h to control the oxygen vacancies on the surface of the TiO_2.

4.3. Characterization

The results of the light-soaking PSC stability test and the photovoltaic performance of the devices with a metallic mask (active area 0.14 cm^2) were measured under solar-simulated light (Oriel Sol 3A class AAA, Newport) using an electrochemical workstation (CHI660, CHI Instrument) system. The AM 1.5 G sun light (100 mA cm^{-2}) was calibrated to a reference Si solar cell (PVM 95). The cross-sectional structures and individual layers of the devices were obtained using a field-emission scanning electron microscope (JSM-7600F, JEOL). The incident photo-to-current conversion efficiency and integrated current of the PSCs were measured through quantum efficiency measurements within a spectra range of 300–800 nm in air under light illumination from a 300 W xenon lamp. The transmittance of the MoO_x/Ag/MoO_x films was examined using a PerkinElmer Lambda 35 UV/vis spectrometer equipped with an integrating sphere. The phase structure of the device was confirmed using X-ray diffraction (PANanalytical Empyrean). The angle ranged from 10° to 40° with a 2θ range. Defects in the PSCs were measured using admittance spectroscopy (AS) at an AC voltage of 30 mV. The frequency and temperature were applied within a frequency sweep ranging from 10^2 to 10^6 Hz, and within a temperature

range of 170 °C–290 °C.

Acknowledgment

This work was supported from the Global Frontier R&D Program on Center for Multiscale Energy System, Korea (2012M3A6A7054855), Ministry of Education, Korea (2018R1D1A1B07050694), and National Science Foundation (NSF 1709307).

Appendix A. Supplementary data

Supplementary data to this article can be found online at https://doi.org/10.1016/j.jpowsour.2019.226768.

References

[1] NREL Chart, www.nrel.gov/pv/assets/images/efficiency-chart-20190423.jpg, accessed: 04, 2019.
[2] J.-W. Lee, D.-H. Kim, H.-S. Kim, S.-W. Seo, S.M. Cho, N.-G. Park, Formamidinium and cesium hybridization for photo- and moisture-stable perovskite solar cell, Adv. Energy Mater. 5 (2015) 1501310.
[3] J.H. Noh, S.H. Im, J.H. Heo, T.N. Mandal, S.I. Seok, Chemical management for colorful, efficient, and stable inorganic-organic hybrid nanostructured solar cells, Nano Lett. 13 (2013) 1764–1769.
[4] M. Saliba, T. Matsui, K. Domanski, J.Y. Seo, A. Ummadisingu, S.M. Zakeeruddin, J. P. Correa-Baena, W.R. Tress, A. Abate, A. Hagfeldt, M. Gratzel, Incorporation of rubidium cations into perovskite solar cells improves photovoltaic performance, Science 354 (2016) 206–209.
[5] M. Saliba, T. Matsui, J.Y. Seo, K. Domanski, J.P. Correa-Baena, M.K. Nazeeruddin, S.M. Zakeeruddin, W. Tress, A. Abate, A. Hagfeldt, M. Gratzel, Cesium-containing triple cation perovskite solar cells: improved stability, reproducibility and high efficiency, Energy Environ. Sci. 9 (2016) 1989–1997.
[6] G.S. Han, H.S. Chung, B.J. Kim, D.H. Kim, J.W. Lee, B.S. Swain, K. Mahmood, J. S. Yoo, N.-G. Park, J.H. Lee, H.S. Jung, Retarding charge recombination in perovskite solar cells using ultrathin MgO-coated TiO_2 nanoparticulate films, J. Mater. Chem. 3 (2015) 9160–9164.
[7] S. Ito, S. Tanaka, K. Manabe, H. Nishino, Effects of surface blocking layer of Sb_2S_3 on nanocrystalline TiO_2 for $CH_3NH_3PbI_3$ perovskite solar cells, J. Phys. Chem. C 118 (2014) 16995–17000.
[8] P. Calado, A.M. Telford, D. Bryant, X. Li, J. Nelson, B.C. O'Regan, P.R. Barnes, Evidence for ion migration in hybrid perovskite solar cells with minimal hysteresis, Nat. Commun. 7 (2016) 13831.
[9] G.S. Han, H.W. Shim, S. Lee, M.L. Duff, J.K. Lee, Low-temperature modification of ZnO nanoparticles film for electron-transport layers in perovskite solar cells, ChemSusChem 10 (2017) 2425–2430.
[10] G.S. Han, H.S. Chung, D.H. Kim, B.J. Kim, J.W. Lee, N.G. Park, I.S. Cho, J.K. Lee, S. Lee, H.S. Jung, Epitaxial 1D electron transport layers for high-performance perovskite solar cells, Nanoscale 7 (2015), 15284-152890.
[11] Y. Guo, J. Jiang, S. Zuo, F. Shi, J. Tao, Z. Hu, X. Hu, G. Hu, P. Yang, J. Chu, Low temperature solution deposited niobium oxide films as efficient electron transport layer for planar perovskite solar cell, Sol. Energy Mater. Sol. Cells 178 (2018) 186–192.
[12] Q. Wang, Q. Dong, T. Li, A. Gruverman, J. Huang, Thin insulating tunneling contacts for efficient and water-resistant perovskite solar cells, Adv. Mater. 28 (2016) 6734–6739.
[13] J. You, L. Meng, T.B. Song, T.F. Guo, Y.M. Yang, W.H. Chang, Z. Hong, H. Chen, H. Zhou, Q. Chen, Y. Liu, N.D. Marco, Y. Yang, Improved air stability of perovskite solar cells via solution-processed metal oxide transport layers, Nat. Nanotechnol. 11 (2016) pp75–81.
[14] J.S. Yoo, G.S. Han, S. Lee, M.C. Kim, M. Choi, H.S. Jung, J.-K. Lee, Dual function of a high-contrast hydrophobic–hydrophilic coating for enhanced stability of perovskite solar cells in extremely humid environments, Nano Res. 10 (2017) 3885–3895.
[15] G.S. Han, J.S. Yoo, F. Yu, M.L. Duff, B.K. Kang, J.-K. Lee, Highly stable perovskite solar cells in humid and hot environment, J. Mater. Chem. 5 (2017) 14733–14740.
[16] A.T. Barrows, R. Masters, A.J. Pearson, C. Rodenburg, D.G. Lidzey, Indium-free multilayer semi-transparent electrodes for polymer solar cells, Sol. Energy Mater. Sol. Cells 144 (2016) 600–607.
[17] Y. Yang, Q. Chen, Y.T. Hsieh, T.B. Song, N.D. Marco, H.P. Zhou, Y. Yang, Multilayer transparent top electrode for solution processed perovskite/Cu(in,Ga)$(Se,S)_2$ four terminal tandem solar cells, ACS Nano 9 (2015) 7714–7721.
[18] X.-L. Ou, M. Xu, J. Feng, H.-B. Sun, Flexible and efficient ITO-free semitransparent perovskite solar cells, Sol. Energy Mater. Sol. Cells 157 (2016) 660–665.
[19] K.O. Brinkmann, J. Zhao, N. Pourdavoud, T. Becker, T. Hu, S. Olthof, K. Meerholz, L. Hoffmann, T. Gahlmann, R. Heiderhoff, M.F. Oszajca, N.A. Luechinger, D. Rogalla, Y. Chen, B. Cheng, T. Riedl, Suppressed decomposition of organometal halide perovskites by impermeable electron-extraction layers in inverted solar cells, Nat. Commun. 8 (2017) 13938.
[20] J. Zhao, K.O. Brinkmann, T. Hu, N. Pourdavoud, T. Becker, T. Gahlmann, R. Heiderhoff, A. Polywka, P. Görrn, Y. Chen, B. Cheng, T. Riedl, Self-encapsulating thermostable and air-resilient semitransparent perovskite solar cells, Adv. Energy Mater. 7 (2017) 1602599.
[21] Y. Zhao, A.M. Nardes, K. Zhu, Effective hole extraction using MoO_x-Al contact in perovskite $CH_3NH_3PbI_3$ solar cells, Appl. Phys. Lett. 104 (2014) 213906.
[22] E.D. Gaspera, Y. Peng, Q. Hou, L. Spiccia, U. Bach, J.J. Jasieniak, Y.-B. Cheng, Ultra-thin high efficiency semitransparent perovskite solar cells, Nano Energy 13 (2015) 249–257.
[23] C. Levard, E.M. Hotze, V. Gregory, G.E. Brown, Environmental transformations of silver nanoparticles: impact on stability and toxicity, Environ. Sci. Technol. 46 (2012) 6900–6914.
[24] M. Jiang, F. Lan, B. Zhao, Q. Tao, J. Wu, D. Gao, G. Li, Observation of lower defect density in $CH_3NH_3Pb(I,Cl)_3$ solar cells by admittance spectroscopy, Appl. Phys. Lett. 108 (2016) 243501.
[25] J.B. Patel, J. Wong-Leung, S. Van Reenen, N. Sakai, J.T.W. Wang, E.S. Parrott, M. Liu, H.J. Snaith, L.M. Herz, M.B. Johnston, Influence of interface morphology on hysteresis in vapor-deposited perovskite solar cells, Adv. Electron. Mater. 3 (2016) 1600470.
[26] H.-S. Duan, H. Zhou, Q. Chen, P. Sun, S. Luo, T.-B. Song, B. Bob, Y. Yang, The identification and characterization of defect states in hybrid organic–inorganic perovskite photovoltaics, Phys. Chem. Chem. Phys. 17 (2015) 112–116.
[27] B. Olyaeefar, S. Ahmadi-Kandjani, A. Asgari, Classical modelling of grain size and boundary effects in polycrystalline perovskite solar cells, Sol. Energy Mater. Sol. Cells 180 (2018) 76–82.
[28] G.S. Han, S. Lee, M.L. Duff, F. Qin, J.K. Lee, Highly bendable flexible perovskite solar cells on a nanoscale surface oxide layer of titanium metal plates, ACS Appl. Mater. Interfaces 10 (2018) 4697–4704.
[29] B.J. Kim, D.H. Kim, Y.-Y. Lee, H.-W. Shin, G.S. Han, J.S. Hong, K. Mahmood, T. K. Ahn, Y.-C. Joo, K.S. Hong, N.-G. Park, S. Lee, H.S. Jung, Highly efficient and bending durable perovskite solar cells: toward a wearable power source, Energy Environ. Sci. 8 (2015) 916–921.